

# Visible light photocatalytic activity and Photoelectrochemical property of Fe-doped TiO<sub>2</sub> hollow spheres by sol–gel method

Xiaoxia Lin · Fei Rong · Xiang Ji · Degang Fu

Received: 7 March 2011 / Accepted: 16 May 2011 / Published online: 1 June 2011  
© Springer Science+Business Media, LLC 2011

**Abstract** Fe-doped TiO<sub>2</sub> hollow spheres (Fe-THs) were synthesized by sol–gel process using carbon spheres as templates. The prepared samples were characterized by X-ray diffraction (XRD), transmission electron microscopy (TEM), UV–vis diffuse reflectance spectrum (DRS), N<sub>2</sub> adsorption–desorption isotherms, Electron paramagnetic resonance (EPR) spectroscopy and Photoluminescence emission spectroscopy (PL). UV–vis spectra showed that Fe<sup>3+</sup> doping could extend the absorption edge to the visible region. EPR spectra showed that Fe<sup>3+</sup> was incorporated into the crystal lattice of TiO<sub>2</sub>, which could inhibit the recombination of photo-induced electron–hole pairs and improve the photocatalytic activity. The photocatalytic activities of the prepared samples were evaluated for the degradation of dye Reactive Brilliant Red X-3B (C.I. reactive red 2) under visible light irradiation. The results indicated that Fe<sup>3+</sup> doping sample showed the highest photocatalytic activity with an optimal doping concentration of 0.50 wt%. The recycle ability of the Fe-THs was also investigated. After 5 cycles, the degradation rate was still higher than 90%, decreased by only 6.36% compared to the first cycle. Moreover, in order to characterize the electron-transferring efficiency in the process of photocatalysis reaction, a photocurrent-time spectrum was examined by anodic photocurrent response.

**Keywords** Titania · Fe-doped · Hollow spheres · Sol–gel · Photocatalysis · Photocurrent

## 1 Introduction

Titanium dioxide (TiO<sub>2</sub>) has been widely used for environment protection (such as water and air pollution) because of its relatively high efficiency, photostability, chemical stability, low cost and non-toxicity [1, 2]. However, its practical application is inhibited for the low photo utilization efficiency and using ultraviolet as excitation source due to the wide band gap of TiO<sub>2</sub> (3.2 eV for anatase) [3]. For the sake of efficient utilization of sunlight, it is necessary to extend the photo-response of TiO<sub>2</sub> to the visible light region. There are many methods for the preparation of visible light responsive photocatalyst such as doping of TiO<sub>2</sub> with metal ions. This method not only extends the photo-response to visible light region, but also inhibits the recombination of photo-induced electron–hole pairs during migration from inside of the material to the surface [4–6]. Among various dopants, Fe<sup>3+</sup> has been found to be an appropriate candidate due to its unique half-filled electronic configuration, which may narrow the energy band gap through the formation of new intermediate energy levels [7]. Many researchers have reported that doping with Fe<sup>3+</sup> exhibits effective photocatalytic activity for the degradation of organic pollutant under visible light irradiation [7–10].

On the other hand, because TiO<sub>2</sub> photocatalysis is surface-mediated advanced oxidation process, the morphology and microstructures are very important to the photocatalytic activity. Enhanced surface exposure to photons and increased mass transfer of target pollutants to the surface of photocatalyst can increase its photonic efficiency

X. Lin · X. Ji · D. Fu (✉)  
State Key Laboratory of Bioelectronics, Southeast University,  
Nanjing 210096, China  
e-mail: fudegang@seu.edu.cn

X. Lin · F. Rong · X. Ji · D. Fu  
Suzhou Key Laboratory of Environment and Biosafety,  
Suzhou 215123, China

or quantum yield. Among different structures, such as nanorods, nanotubes and hollow spheres [11–13], hollow spheres structures have attracted enormous attention because of their low density, high surface area, high energy conversion efficiency as well as large light-harvesting efficiencies. High surface area associated with hollow structure can allow pollutant access to both exterior and interior photocatalyst surfaces, while low bulk density can make homogeneous dispersion throughout the photo reactor volume [14].

Sun et al. [15] reported the preparation of colloid carbon spheres, which could be used as templates to prepare metal oxides hollow spheres. The surface modification is unnecessary because the surface of colloid carbon spheres is hydrophilic and has a distribution of –OH and –C=O groups. Kuang et al. [16] prepared Fe-doped Titania hollow spheres by hydrothermal precipitation. However, to the best of our knowledge, there is no report on Fe-THs prepared using carbon spheres as templates by a simple sol-gel process. In this study, for the achievement of visible light responsive  $\text{TiO}_2$  with high photocatalytic activity, we prepared Fe-THs by sol–gel process using carbon spheres as templates. The photocatalytic activities were evaluated by degradation of Reactive Brilliant Red dye X-3B in aqueous solution under visible light irradiation. The recycle ability of the Fe-THs was also investigated. Moreover, in order to characterize the electron-transferring efficiency in the process of photocatalysis reaction, a photocurrent-time spectrum was examined by anodic photocurrent response.

## 2 Experimental

### 2.1 Preparation of carbon spheres

9 g glucose was firstly dissolved in 70 mL water to form a clear solution. The solution was then sealed in a 100 mL Teflon-lined stainless autoclave and maintained at 453 K for 5 h. The samples were then washed by ethanol and water for five cycles, respectively. The obtained carbon spheres were then dried at 353 K for 2 h under vacuum.

### 2.2 Synthesis of Fe-doped $\text{TiO}_2$ hollow spheres (Fe-THs)

$\text{Ti(OBu)}_4$  and  $\text{Fe(NO}_3)_3$  were used as starting materials. Fe-THs were prepared by sol–gel method [17]. In a typical synthesis, definite  $\text{Fe(NO}_3)_3$  was dissolved into the mixture of 48 mL absolute ethanol and 0.5 g distilled water, and then 0.3 g carbon spheres were added. In our experiment, Fe doping content was chosen as 0, 0.25, 0.50, and 1.0 wt%, which was the mass percentage of  $\text{Fe}^{3+}$  in the  $\text{TiO}_2$  hollow spheres (THs) powders. The corresponding samples

were marked as THs, 0.25Fe-THs, 0.50Fe-THs, and 1.0Fe-THs, respectively.  $\text{Ti(OBu)}_4$  diluted with absolute ethanol was added dropwise into the above suspension under vigorous stirring. Then, the solution was stirred rapidly at 353 K for 6 h. Finally the products were centrifuged, washed and redispersed in ethanol and water for three cycles. In order to prepare Fe-THs, the  $\text{TiO}_2$ -carbon spheres composite particles were calcined at 773 K for 3 h (ramped up at 5 K/min) to remove the carbon spheres cores.

### 2.3 Photocatalysts characterization

The X-ray diffraction (XRD) patterns obtained on a X-ray diffractometer (XD-3A, Shimadzu Corporation, Japan) using  $\text{CuK}\alpha$  irradiation at 40 kV, 30 mA over the  $2\theta$  range 20–80° were used to determine the identity of any phase present and their crystallite size. The size and morphology were observed by transmission electron microscopy (TEM, JEM2000EX). A UV-vis spectrophotometer (Shimadzu UV-8500) was used to record the diffuse reflectance spectra (DRS) of samples. Nitrogen adsorption–desorption isotherms were collected at 77 K using an ASAP2020 instrument (BET and BJH models for specific surface area and porosity evaluation) for samples. Prior to measurement, all samples were degassed at 423 K for 5 h. Electron paramagnetic resonance (EPR, Bruker ER200D) measurement at 77 K was operated at X-band frequency of 9.2 GHz in solid state itself. The photoluminescence emission spectra of the samples were measured at room temperature by a LS-55 (Perkin Elmer) devise.

### 2.4 Photoelectrochemical and photocatalytic studies

The photoelectrochemical property was measured with a CHI660 electrochemical workstation (CH Instruments Inc, USA). A standard three-electrode system equipped with a quartz window was used in experiments. An optically transparent  $\text{In}_2\text{O}_3$ – $\text{SnO}_2$  oxide conductive glass sheet was used to working electrode and 0.01 M  $\text{Na}_2\text{SO}_4$  was used to supporting electrolyte. A Pt plate was used as cathode and a saturated calomel electrode (SCE) was used as a reference electrode. The reaction solution was 30 mL mixture of X-3B with a concentration of 25 mg L<sup>−1</sup> and 1.0 g L<sup>−1</sup> different photocatalysts and the working electrode were dipped into the solution. After 1 h, the X-3B molecules and  $\text{TiO}_2$  particles in the solution were adsorbed on the surface of the working electrode, the visible light was turned on to illuminate the working electrode from the front side.

The photocatalytic activities of the prepared samples were determined by degradation of X-3B in aqueous solution under visible light irradiation. The dye with reagent grade was used without further purification and its

molecular structure was illustrated in Fig. 8 inset. A 250 W halogen lamp (Instrumental Corporation of Beijing Normal University) at upper surface of the reactor with a light filter cutting the light below 420 nm was used as visible light source with an average irradiation intensity of  $9 \text{ mW cm}^{-2}$ . A set of photocatalytic degradation experiments were performed following this procedure: 0.2 g catalyst was merged into the X-3B solution with a volume of 200 mL and an initial concentration of  $50 \text{ mg L}^{-1}$ . Prior to photoreaction, air was pumped into the reactor in the dark for 30 min to reach adsorption–desorption equilibrium. At a definite time interval, 5 mL suspension was collected, and then the concentration of X-3B was analyzed using the UV-vis spectrophotometer at 535 nm. The blank experiment without catalysts was also investigated, and the value could be neglected with only 2.2% of conversion after 2 h irradiation.

### 3 Results and discussion

#### 3.1 Characterization of Fe-doped $\text{TiO}_2$ hollow spheres

Figure 1 shows XRD patterns of undoped and  $\text{Fe}^{3+}$ -doped  $\text{TiO}_2$  samples. It can be seen that all samples exhibit only the characteristic peaks of anatase phase (major peaks:  $25.4^\circ$ ,  $38.2^\circ$ ,  $48.2^\circ$ ,  $54.7^\circ$ ). Any other crystalline phase ( $\text{Fe}_2\text{O}_3$  or  $\text{Fe}_x\text{TiO}_y$ ) could not be observed, which reveals that the Fe content of our samples is below the detection limits of the XRD instrument, or the iron ions may substitute titanium on the  $\text{TiO}_2$  matrix or be located interstitially forming a  $\text{Fe}-\text{TiO}_2$  solid solution due to the similar ionic radius of  $\text{Fe}^{3+}$  and  $\text{Ti}^{4+}$  [8, 18]. The crystal size of THs is estimated by applying the Scherrer equation

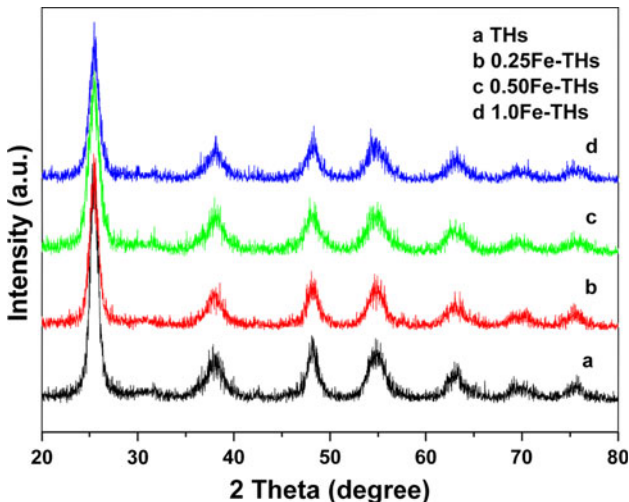


**Fig. 1** XRD patterns of THs, 0.25Fe-THs, 0.50Fe-THs and 1.0Fe-THs

( $D = k\lambda/\beta \cos\theta$ ), where  $D$  is crystal size,  $\lambda$  is the wavelength of the X-ray irradiation,  $k$  is the Scherrer constant ( $k = 0.899$ ),  $\theta$  is the diffraction angle and  $\beta$  is the full-width-at-half-maximum of the (101) plane (in radians) [3]. The mean crystallite size of THs, 0.25Fe-THs, 0.50Fe-THs, and 1.0Fe-THs are 11.98, 11.25, 10.56, 9.92 nm, respectively. The effect of iron doping on crystallite size is still under debate and subject to some controversy. Some investigators have reported that doping with  $\text{Fe}^{3+}$  increases the crystallite size [19, 20] while some research groups have found that the presence of this  $\text{Fe}^{3+}$  in  $\text{TiO}_2$  decreases the crystallite size [21, 22]. In our study, the crystallite size of iron doped samples is slightly lower than that of THs. This decrease is caused by a number of defects in the anatase crystallites produced by the substitution of part of the  $\text{Ti}^{4+}$  site by  $\text{Fe}^{3+}$ , which may retard crystallite growth [21].

The TEM image of carbon spheres is shown in Fig. 2a. It can be seen that diameter of carbon spheres ranges from 200 to 350 nm. TEM image of 0.50Fe-THs is shown in Fig. 2b. A contrast between the centers and the edges indicates that the hollow structure of  $\text{TiO}_2$  has been formed. Diameter of the hollow spheres ranges from 200 to 300 nm and the shell thickness is about 30 nm.

The UV-vis spectra of the prepared samples are shown in Fig. 3. The results show that  $\text{Fe}^{3+}$  doping can effectively

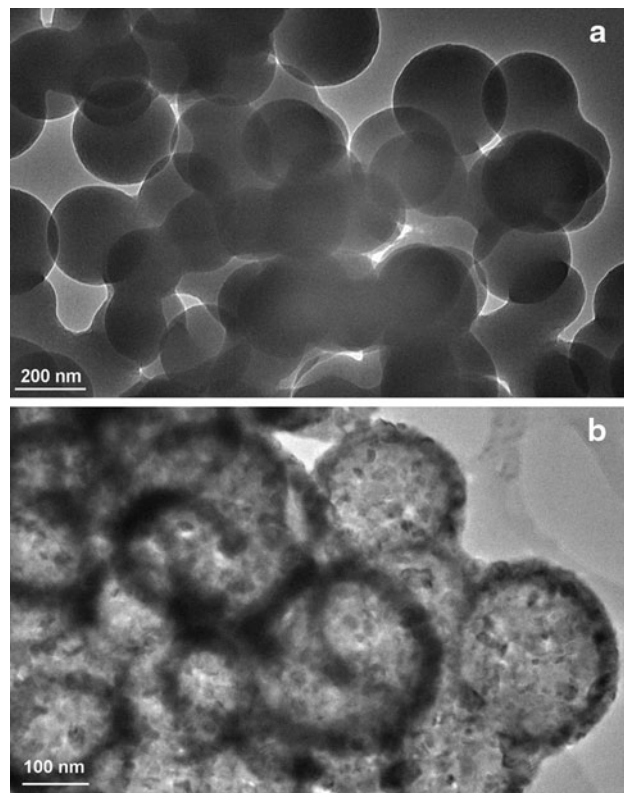


**Fig. 2** TEM images of **a** carbon spheres and **b** 0.50Fe-THs

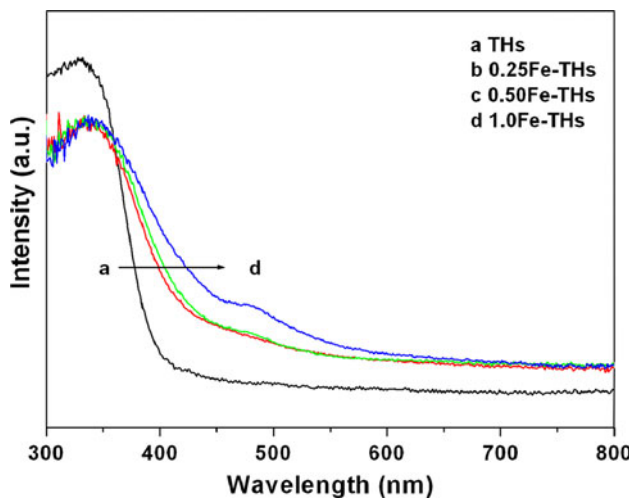


**Fig. 3** The diffuse reflectance UV-vis spectra of THs, 0.25Fe-THs, 0.50Fe-THs and 1.0Fe-THs

**Table 1** Surface area measurement and band gap energies  $E_g$  of the different samples

Samples	BET surface area ( $\text{m}^2/\text{g}$ )	Pore volume ( $\text{cm}^3/\text{g}$ )	Band gap energy (eV)
THs	279.18	0.261	3.13
0.25Fe-THs	296.35	0.281	2.93
0.50Fe-THs	312.62	0.286	2.89
1.0Fe-THs	327.83	0.292	2.71

shift the absorption spectrum into the visible region. The intensity of visible absorbance of hollow spheres increases with increasing the doped amount of iron. Furthermore, the relation between absorption coefficient ( $\alpha$ ) and incident photon energy ( $h\nu$ ) can be written as  $\alpha h\nu = B_d(h\nu - E_g)^n$  for allowed transitions ( $n = 2$  for indirect transition), where  $B_d$  is the absorption constants [23]. The intercept of the tangent to the  $(\alpha h\nu)^{1/2}$  versus  $h\nu$  plots could give an estimation of the band gap energies for the samples [24]. Table 1 presents the energy band gaps ( $E_g$ ) of the photocatalysts. The reduction of  $E_g$  attributes to the presence of Fe [8]. Yamashita and co-workers indicated that in metal ion-implanted  $\text{TiO}_2$  the overlap of the conduction band due to Ti(d) of  $\text{TiO}_2$  and the metal(d) orbital of the implanted metal ions could decrease the band gap of  $\text{TiO}_2$  [25, 26].

Figure 4 shows the typical plot of nitrogen adsorption–desorption isotherm and pore size distribution (inset) of 0.50Fe-THs. The sample shows an isotherm of type IV with hysteresis loop, which indicates the existence of mesoporous structure of  $\text{TiO}_2$  hollow spheres. The hollow spheres show bimodal pore size distribution, which contain small mesopores and large mesopores. The smaller mesopores are related to finer intra-aggregated pores formed between primary particles, and the larger are associated

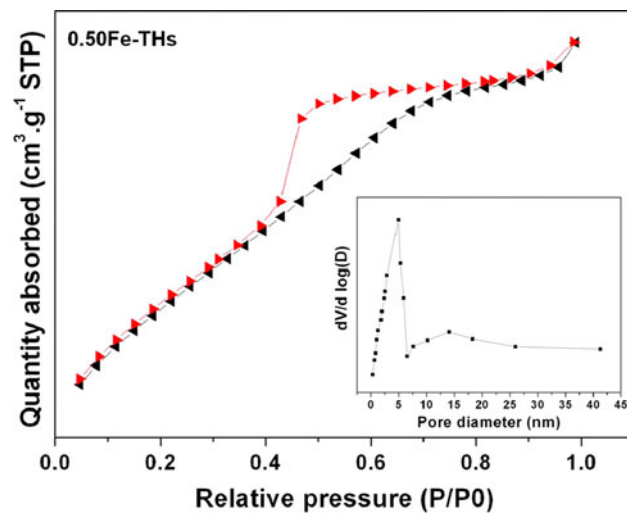


**Fig. 4** Nitrogen adsorption–desorption isotherm and pore size distribution (inset) of 0.50Fe-THs

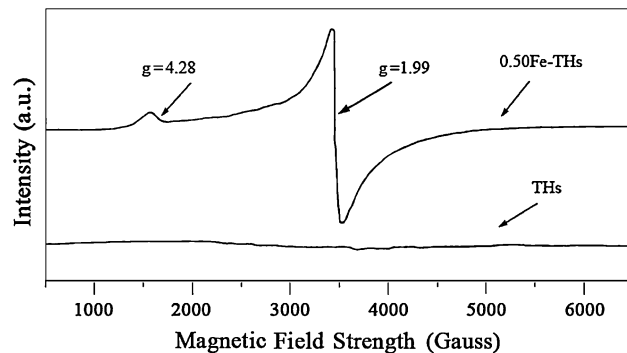


**Fig. 5** Electron paramagnetic resonance spectra of THs and 0.50Fe-THs

with inter-aggregated pores produced by inter-aggregated secondary constructs. This bimodal mesopores size distribution is beneficial to light-harvesting and mass transport [27, 28]. Table 1 summarizes the results of different samples calculated based on  $\text{N}_2$  adsorption–desorption isotherms. From Table 1 we can see that all the samples have large surface areas and similar values of the pore volumes, such similarities in physicalchemical properties make it convenient to study the effects of  $\text{Fe}^{3+}$  on the performance of  $\text{TiO}_2$  hollow spheres.

Electron paramagnetic resonance (EPR) spectroscopy has been used to investigate the iron doped  $\text{TiO}_2$  sample, which is a highly sensitive technique for examining paramagnetic species and can give valuable information about the lattice site. The typical EPR spectrum of 0.50Fe-THs is shown in Fig. 5. The sample after iron doping shows intense signal at  $g = 1.99$  and weak signal at  $g = 4.28$ , however, there are no signals of paramagnetic species for the THs. The intense signal at  $g = 1.99$  can be attributed to

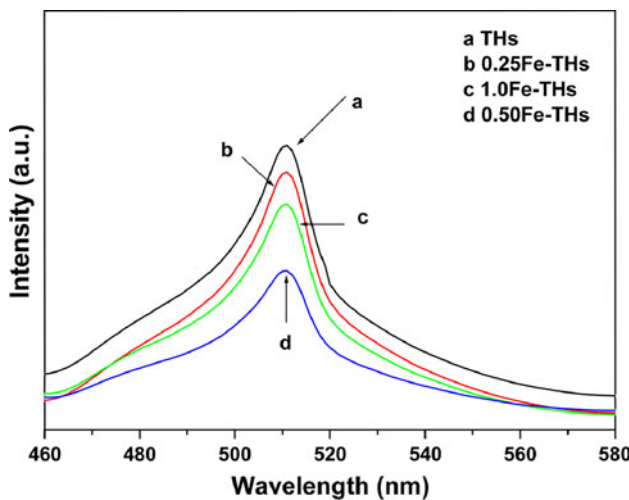


**Fig. 6** PL spectra of THs, 0.25Fe-THs, 0.50Fe-THs and 1.0Fe-THs

Fe<sup>3+</sup> substituted Ti<sup>4+</sup> in the TiO<sub>2</sub> lattice, while the weak signal at  $g = 4.28$  should be ascribed to Fe<sup>3+</sup> substituted in the lattice adjacent to a charge-compensating oxide anion vacancy [29–31]. The EPR result confirms that Fe<sup>3+</sup> is successfully incorporated into the crystal lattice of THs.

Photoluminescence emission spectra (PL) have been widely used to investigate the efficiency of charge trapping, immigration, transfer and to understand the fate of electron–hole pairs [32]. In this study, the PL emission spectra of the several samples are shown in Fig. 6. It can be seen that the PL intensities of 0.50Fe-THs is the lowest among all samples. Because the PL emission results from the recombination of photo-induced electron–hole pairs, the lower PL intensity means the lower recombination rate of electron–hole pairs and higher photocatalytic activity [33, 34].

### 3.2 Photoelectrochemical property

The photocurrent response measurement is carried out under visible light irradiation to further investigate the photo-induced charges separation efficiency of undoped and Fe-doped samples in solution. The working electron potentials are located at 0 V versus the saturated calomel electrode and the results are shown in Fig. 7. From the results we can see that the photocurrent of Fe-THs is higher than THs during visible light irradiation. This difference may be attributed to that THs can be sensitized only by X-3B under visible light irradiation with electrons transferring from excited X-3B to the conduct band of THs, while Fe-THs can still be excited to generate electrons and holes by photons besides X-3B sensitizing. Higher photocurrent means more photo-induced electrons can transfer to counter electrode from Fe-THs via external circuit efficiently. We can forecast that the Fe-THs would show

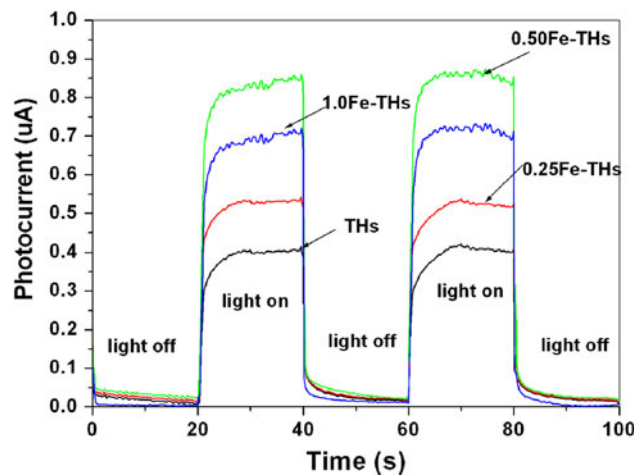


**Fig. 7** Photocurrent response of THs, 0.25Fe-THs, 0.50Fe-THs and 1.0Fe-THs

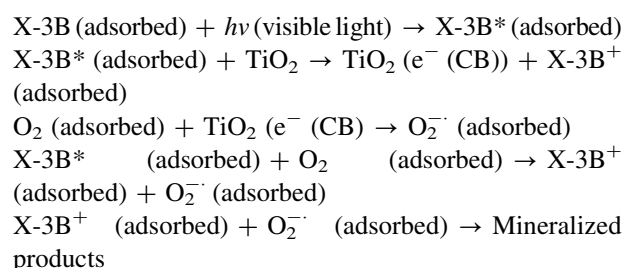
**Table 2** Absorption and degradation parameters of X-3B by different samples

Samples	Amount of X-3B adsorbed on TiO <sub>2</sub> samples (mol/g-TiO <sub>2</sub> )	Degradation percent (%)	$K_{app}$ (min <sup>-1</sup> )
P25	$8.35 \times 10^{-6}$	12.2	$9.88 \times 10^{-4}$
THs	$2.29 \times 10^{-5}$	38.1	0.00422
0.25Fe-THs	$2.33 \times 10^{-5}$	75.3	0.0118
0.50Fe-THs	$2.35 \times 10^{-5}$	96.7	0.0288
1.0Fe-THs	$2.36 \times 10^{-5}$	83.2	0.0153

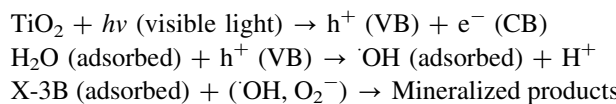
higher photocatalytic activity than THs under visible light region.

### 3.3 Photocatalytic activity

To investigate the photocatalytic activity of TiO<sub>2</sub> hollow spheres, X-3B was used as a model pollutant. The adsorption–desorption of X-3B on TiO<sub>2</sub> hollow samples was tested in the dark at room temperature, and the results are shown in Table 2. For comparison, the activities of P25 and THs were also evaluated under the identical conditions. The proposed photocatalytic process illuminated with visible light for P25 and THs may be shown as follows [35, 36]:



For Fe-THs, there exists a direct photocatalysis under visible light irradiation:



The results are shown in Fig. 8. The apparent rate constant ( $k_{app}$ ) is chosen as the basic kinetic parameter for evaluation of different photocatalysts [3, 37]. The apparent rate constant is calculated by the following equation:  $\ln(C_0/C) = k_{app} \times t$ . Where  $C_0$  represents the initial concentration,  $t$  is reaction time and  $C$  is the X-3B concentration in the solution. The  $k_{app}$  data are listed in Table 2. It can be seen that the  $k_{app}$  of Fe-THs obviously increases under visible light irradiation compared to P25 and THs. Since the stability of catalysts is one of key steps to make practical applications for this heterogeneous photocatalysis technology. An examination of cyclic ability of the Fe-THs was also carried out under visible light irradiation. The results are shown in Fig. 9. After 5 cycles, the degradation rate is still higher than 90%, decreased by only 6.36%, which suggests that Fe-THs would be a potential photocatalyst for this reaction.

The high photocatalytic activity of Fe-THs is probably due to the following reasons. Firstly, it is generally accepted that the catalytic process is related to the adsorption and desorption of molecules on the surface of the catalyst. The larger surface area of hollow spheres may induce more reactant adsorption/desorption sites for catalytic reaction. Secondly,  $\text{Fe}^{3+}$  can make a red shift in band gap transition and enhance the intensity of absorption in the visible light region. Meanwhile,  $\text{Fe}^{3+}$  ions at an appropriate doping concentration can also inhibit the recombination of photo-induced carriers and improve the photocatalytic

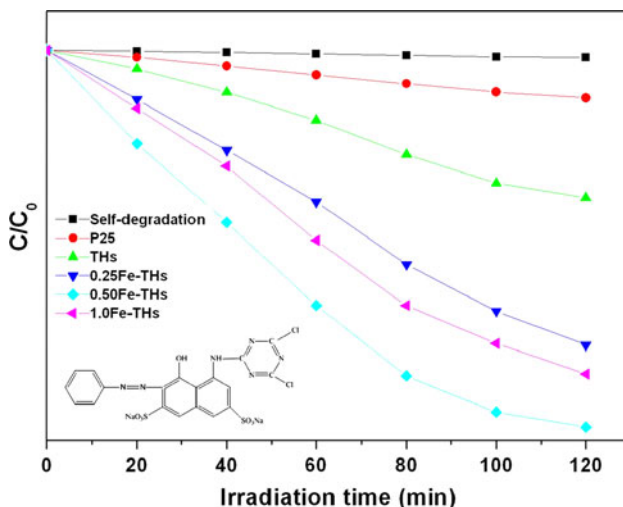


**Fig. 8** Kinetic of X-3B degradation for different samples and chemical structure of X-3B (inset),  $C_0$  and  $C$  represent the initial concentration of X-3B and concentration at time  $t$ , respectively

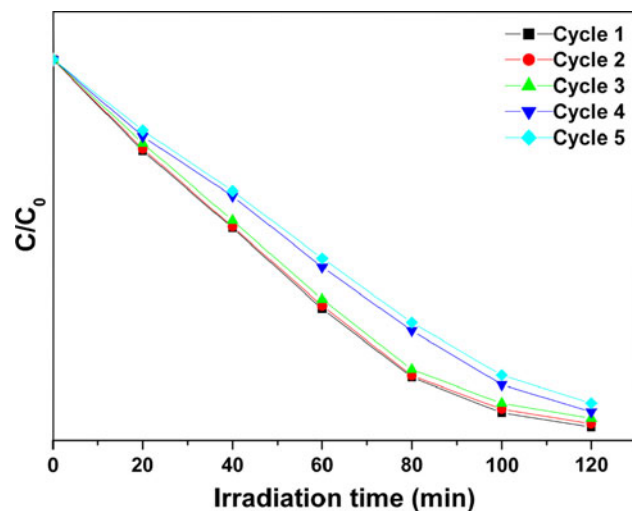


**Fig. 9** Cycles of the photocatalytic activity of X-3B in the presence of 0.50Fe-THs

activity [38]. Similar observation has been reported previously [19]. Zhang et al. [19] demonstrated that Fe-doped  $\text{TiO}_2$  sample could show higher photocatalytic activity by controlling dopant concentration. In our experiment while the dopant amount of iron exceeds 0.50 wt%, the photocatalytic activity decreases instead, though there is still an increase in the absorbance of the visible light region, which is consistent with the PL and photocurrent results. At high concentration, superfluous iron ions in the  $\text{TiO}_2$  sample may act as recombination center, resulting in the decreasing photocatalytic activity [26, 39].

#### 4 Conclusions

In summary, we prepared Fe-doped  $\text{TiO}_2$  hollow spheres by sol-gel process using carbon spheres as templates. The results show that the doped samples shift remarkably to the visible light region and the absorption enhances significantly. The photocatalytic activities of the prepared samples under visible light irradiation was compared to that of commercial P25 powders and undoped  $\text{TiO}_2$  hollow spheres by photocatalytic degradation of X-3B. The results indicate that  $\text{Fe}^{3+}$  doping shows the highest photocatalytic activity with an optimal doping concentration of 0.50 wt%. An examination of cyclic ability of the Fe-THs was also carried out under visible light irradiation. After 5 cycles, the degradation rate is still higher than 90%, decreased by only 6.36%, which suggests that Fe-THs would be a potential photocatalyst for this reaction.

**Acknowledgments** This work is financially supported from the National Science Foundation of China (No. 30670522), the Hi-Tech Research and Development Program (863 Program) of China (No.

2006AA10Z436) and Social Developing Program of Jiangsu Province (BE2008643).

## References

1. Fujishima A, Rao TN, Tryk DA (2000) *J Photochem Photobiol* 1:1–21
2. Cozzoli PD, Kornowski A, Weller H (2003) *J Am Chem Soc* 125:14539–14548
3. Wang C, Ao YH, Wang PF, Hou J, Qian J, Zhang SH (2010) *J Hazard Mater* 178:517–521
4. Akbarzadeh R, Umbarkar SB, Sonawane RS, Takle S, Dongare MK (2010) *Appl Catal A* 374:103–109
5. Sasikala R, Sudarsan V, Sudakar C, Naik R, Sakuntala T, Bharadwaj SR (2008) *Int J Hydrogen Energy* 33:4966–4973
6. Fan XX, Chen XY, Zhu SP, Li ZS, Yu T, Ye JH, Zou ZG (2008) *J Mol Catal A Chem* 284:155–160
7. Zhu J, Ren J, Huo YN, Bian ZF, Li HX (2007) *J Phys Chem C* 111:18965–18969
8. Castro-López CA, Centeno A, Giraldo SA (2010) *Catal Today* 157:119–124
9. Khan MA, Woo SI, Yang OB (2008) *Int J Hydrogen Energy* 33:5345–5351
10. Cui LF, Huang F, Niu MT, Zeng LW, Xu J, Wang YS (2010) *J Mol Catal A Chem* 326:1–7
11. Monteleone FV, Caputo G, Canale C, Cozzoli PD, Cingolani R, Fragouli D, Athanassiou A (2010) *Langmuir* 26:18557–18563
12. Deng LX, Chen YL, Yao MY, Wang SR, Zhu BL, Huang WP, Zhang SM (2010) *J Sol-Gel Sci Technol* 53:535–541
13. Jin L, Xu LP, Morein C, Chen CH, Lai M, Dharmarathna S, Dobley A, Suib SL (2010) *Adv Funct Mater* 22:3373–3382
14. Subagio DP, Srinivasan M, Lim M, Lim TT (2010) *Appl Catal B* 95:414–422
15. Sun X, Li Y (2004) *Angew Chem Int Ed Engl* 43:597–601
16. Kang JD, Lin BZ, Chen YL, Pian XT, Zhang KZ, Zhang O (2010) *Chin J Catal* 31:1399–1404
17. Ao YH, Xu JJ, Fu DG, Yuan CW (2008) *Catal Commun* 9:2574–2577
18. Wang CY, Bottcher C, Bahneman DW, Dohrman JK (2003) *J Mater Chem* 13:2322–2325
19. Zhang ZB, Wang CC, Zakaria R, Ying JK (1998) *J Phys Chem B* 102:10871–10878
20. Cong Y, Zhang JL, Chen F, Anpo M, He DN (2007) *J Phys Chem C* 111:10618–10623
21. Wu YM, Zhang JL, Xiao L, Chen F (2009) *Appl Catal B* 88:525–532
22. Vijayan P, Mahendiran C, Suresh C, Shanthi K (2009) *Catal Today* 141:220–224
23. Wu ZB, Dong F, Liu Y, Wang HQ (2009) *Catal Commun* 11:82–86
24. Yu JG, Xiong JF, Cheng B, Liu SW (2005) *Appl Catal B* 60:211–221
25. Yamashita H, Harada M, Misaka J, Takeuchi M, Ikeue K, Anpo M (2002) *J Photochem Photocatol A* 148:257–261
26. Cai L, Liao XP, Shi B (2010) *Ind Eng Chem Res* 49:3194–3199
27. Yu JG, Yu JC, Leung MKP, Ho WK, Cheng B (2007) *J Catal* 217:69–78
28. Ho WK, Yu JC, Lee SC (2006) *Chem Commun* 10:1115–1117
29. Pecchi G, Reyes P (2003) *J Sol-Gel Sci Technol* 27:205–214
30. Nagaveni K, Hegde MS, Madras G (2004) *J Phys Chem B* 108:20204–20212
31. Ozaki H, Iwamoto S, Inoue M (2007) *J Phys Chem C* 111:17061–17066
32. Yamashita H, Harada M, Misaka J, Takeuchi M, Neppolian B, Anpo M (2003) *Catal Today* 84:191–196
33. Wu YM, Liu HB, Zhang JL, Chen F (2009) *J Phys Chem C* 113:14689–14695
34. Gao B, Ma Y, Cao Y, Yang W, Yao J (2006) *J Phys Chem B* 110:14391–14397
35. Xie YB, Yuan CW (2003) *Appl Catal B* 46:251–259
36. Kumbhar A, Chumanov G (2005) *J Nanopart Res* 7:489–498
37. Matos J, Laine J, Herrmann JM (2001) *J Catal* 200:10–20
38. Liu S, Liu XP, Chen YS, Jiang RY (2010) *J Alloys Compd* 506:877–882
39. Abazovic ND, Mirenghi L, Jankovic IA, Bibic N, Sojic DV, Abramovic BF, Comor MI (2009) *Nanoscale Res Lett* 4:518–525